Nuclear Instruments and Methods in Physics Research A 343 (1994) 494–507
North-Holland

NUCLEAR INSTRUMENTS & METHODS IN PHYSICS RESEARCH
Section A

Linearly polarized photons at MAMI (Mainz) **

D. Lohmann [a,***], J. Peise [b,#], J. Ahrens [b], I. Anthony [c], H.-J. Arends [b], R. Beck [b], R. Crawford [c], A. Hünger [a], K.H. Kaiser [b], J.D. Kellie [c], Ch. Klümper [b], P. Krahn [b], A. Kraus [a], U. Ludwig [b], M. Schumacher [a,*], O. Selke [a], M. Schmitz [b], M. Schneider [b], F. Wissmann [b], S. Wolf [a]

[a] *Zweites Physikalisches Institut der Universität Göttingen, Germany*
[b] *Institut für Kernphysik der Universität Mainz, Germany*
[c] *Department of Physics and Astronomy, The University of Glasgow, UK*

(Received 25 November 1993)

Coherent bremsstrahlung is produced using the 855 MeV electron beam of the Mainz three-stage racetrack microtron MAMI and a diamond crystal inserted as a radiator into the MAMI tagging system. By counting only the electrons on the tagger ladder an intensity spectrum ranging from 50 MeV to 800 MeV was obtained with good statistical accuracy in a running time of 2 s. This short running time makes it possible to measure a complete intensity pattern versus photon energy for different orientations of the diamond crystal in about 15 minutes. By comparing these measured intensity patterns with calculations it becomes possible to precisely align the crystal axes with respect to the axes of the goniometer. Relative intensities of coherent bremsstrahlung are determined experimentally by normalizing the diamond data to data obtained with an amorphous Ni radiator. Good agreement is obtained between experiment and prediction when taking into account the beam divergence, multiple scattering of electrons in the radiator, the Z dependence of the bremsstrahlung spectrum and the finite Debye temperature of diamond. With a collimated photon beam having an aperture of half the characteristic angle degrees of linear polarization appear to be possible ranging from 80% at 200 MeV over 65% at 300 MeV and 55% at 400 MeV to 35% at 500 MeV.

1. Introduction

Linearly polarized photons are a valuable tool for studies in intermediate energy photonuclear reactions because of the enhancement of the sensitivity of the reaction cross sections to the multipolarity of the electromagnetic transition. As an example we mention the determination of the E2/M1 multipolarity ratio for the $p \rightarrow \Delta$ transition of reactions like Compton scattering and π^0 photo production. Though there are backscattered laser beams available providing degrees of linear polarization of 75% to 90% at energies up to 314 MeV [1–3] it is of interest to investigate also the possibility of using coherent bremsstrahlung sources which up to now were believed to provide considerably smaller degrees of linear polarization on a sizeable background of unpolarized photons. The advantages of coherent bremsstrahlung under discussion here are (i) the stability and intensity of the photon beam and (ii) the higher available energy. Furthermore, in the following we show that refinements of the method making use of proper beam alignments and collimation will lead to degrees of linear polarization and polarized to unpolarized intensity ratios which are comparable to those reported for backscattered laser light.

Following earlier work, a first approach to calculate coherent bremsstrahlung in the Born approximation was published by Überall [4,5], who presented formulae for the intensity change of the Bethe–Heitler spectrum due to interference effects on bremsstrahlung production in a single crystal. Later, Überall also showed [6,7] that the photon beam from a crystal has a strong linear polarization for certain orientations. Essential progress was made in experiments by Diambrini et al. at Frascati using 1 GeV electrons [8]. In contrast to the smooth energy dependence of the enhancement predicted by Überall [5] a spectrum was observed with a number of sharp peaks, which were explained [8] by the discrete structure of the reciprocal lattice of the crystal. Further experimental investigations were carried out in Tokio [9] with bremsstrahlung from silicon crystals at 0.6 GeV and at DESY (Hamburg) with 6

* Corresponding author.
** Supported by Deutsche Forschungsgemeinschaft (SFB 201).
*** Excerpt of Diploma Thesis Göttingen 1993, present address: GKSS Forschungszentrum Geesthacht, Germany.
# Diploma Thesis KPH 16, Mainz (1989).

SSDI 0168-9002(93)E1292-6

GeV electrons and diamond [10] and in other laboratories. In 1963 Mozley and De Wire [11] pointed out that collimation of the photon beam reduces the incoherent background whereas the linear polarization and intensity of the coherent spectrum remains unmodified. Calculations of this effect were carried out by refs. [12,13] and some experimental evidence was reported by ref. [14].

Following these early developments, there has been a widespread application of the linear polarization of coherent bremsstrahlung in measurements of the beam asymmetry Σ of photomeson cross sections described in compilations of refs. [15], [16] and [17].

Irrespective of this great interest in and widespread application of the method, the data obtained with linearly polarized coherent bremsstrahlung are not very accurate up to now. Therefore, it may be considered favourable that the 100% duty-factor electron beam installed in Mainz opens a new era in this field of research, because intensity spectra of coherent photons versus photon energy can now be measured within seconds and, therefore, intensity patterns as a function of crystal orientation become an easy method of aligning the crystal and finding the optimum orientation for linear polarization. Taking advantage also of beam collimations we expect substantial improvement on the quality of the beam of linearly polarized photons.

2. Properties of coherent bremsstrahlung

In this section we restrict ourselves to describe those properties of coherent bremsstrahlung production which are of importance for the understanding of the present experiments. For further information we refer to review articles [18–21].

We use the natural unit system $\hbar = c = m = 1$ except for those cases where we write these quantities explicitly. In this unit system (E_0, p_0) denotes energy and momentum of the incident electron, (E, p) energy and momentum of the outgoing electron, k the energy of the produced photon and q the momentum transferred to the crystal. Furthermore, we introduce the fractional photon energy $x = k/E_0$. The production of coherent bremsstrahlung is governed by the momentum transfer q which on the one hand has to fulfill the "pancake" condition as a general constraint and on the other hand depends on the orientation of the momentum transfer q in the reciprocal lattice space. To a good approximation the pancake condition [18–21] is given by the relations

$$\delta \leqslant q_l \leqslant 2\delta, \tag{1}$$

$$0 \leqslant q_t \leqslant 2x, \tag{2}$$

where q_l is the longitudinal component of q and q_t the transverse component of q. The quantity $\delta = q_l^{\min}$ is the minimum longitudinal momentum transfer, being in agreement with the kinematics of coherent bremsstrahlung production, and is given by

$$\delta = \frac{1}{2E_0}\frac{x}{1-x}. \tag{3}$$

The influence of the crystal structure is given by the Laue condition

$$q = g, \tag{4}$$

where

$$q = p_0 - p - k, \tag{5}$$

is the momentum transferred to the crystal and

$$g = \sum_{k=1}^{3} h_k b_k, \tag{6}$$

the reciprocal lattice vector. In Eq. (6) h_k are the Miller indices and b_k the basis vectors of the reciprocal lattice. The pancake condition implies that a reciprocal lattice vector cannot contribute to the cross section when it is leaving the pancake as a consequence of an increase of the fractional photon energy x. This leaving the pancake leads to a discontinuity in the intensity at the fractional photon energy

$$x_d = \frac{2E_0\delta}{1+2E_0\delta}. \tag{7}$$

Maximum linear polarization is found in the plane (g, p_0) where g is the reciprocal lattice vector responsible for the production of coherent bremsstrahlung and p_0 the momentum of the incident electron.

3. Apparatus

The 855 MeV electron beam of MAMI hits the radiator at the entrance of the tagging magnet (Fig. 1) (Glasgow–Mainz [22]). The radiator is installed in the three-axis goniometer shown in Fig. 2. Three stepmotor drives may be used to carry out rotations around a vertical axis V, a horizontal axis H and an azimuthal axis A. The angle Φ_V of the vertical axis is varied by rotating an outer vertical cylinder, the angle Φ_H of the horizontal axis by rotating an inner vertical cylinder and transforming the vertical rotation into a horizontal one via gear rims. The axial rotation is performed by transforming the vertical rotation of the central axis into a rotation of a metal ring around its normal axis A via a worm gear. The radiator for the production of coherent bremsstrahlung is a diamond crystal mounted in this metal ring with its [100] axis parallel to the A axis.

Further details of the arrangement are described in Fig. 3. The direction of the vertical axis V is fixed in

space and properly aligned perpendicular to the direction of the momentum vector p_0 of the incident electrons. The direction of the horizontal axis H is in its zero position when it is perpendicular to p_0 and can be rotated within the horizontal plane by varying Φ_V. The direction of the azimuthal axis A is in its zero position when it is parallel to p_0 and can be rotated within a vertical plane by varying Φ_H. The horizontal projection of A can be rotated within a horizontal plane by varying Φ_V. According to our definition the diamond crystal is in its zero position when the crystal axes [010] b_2, [001] b_3 and [100] b_1 coincide with the goniometer axes V, H and A, respectively, while the latter are in their zero positions.

The intensity and degree of linear polarization of coherent bremsstrahlung depends on three crystal angles denoted by α, θ and φ. Angle θ is the polar angle and α the azimuth of p_0 in the reference frame of the crystal axes. Angle φ is the azimuth of the reciprocal lattice vector g being responsible for the production of coherent bremsstrahlung, i.e. $q = g$, in the same reference frame. In this reference frame δ can be written

$$\delta = g_1 \cos\theta + \sin\theta(g_2 \cos\alpha + g_3 \sin\alpha), \tag{8}$$

so that the discontinuity in the spectra occurs at

$$x_d = \left[2E_0(g_1 \cos\theta + \sin\theta(g_2 \cos\alpha + g_3 \sin\alpha))\right] \times \left[1 + 2E_0(g_1 \cos\theta + \sin\theta(g_2 \cos\alpha + g_3 \sin\alpha))\right]^{-1}. \tag{9}$$

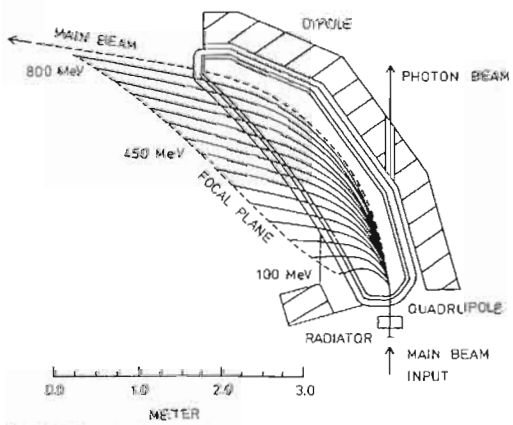

Fig. 1. The tagging system at MAMI. The 855 MeV electron beam hits the radiator at the entrance of the tagging magnet. The radiator is a diamond crystal producing coherent bremsstrahlung superimposed by a background due to incoherent photons. This background is measured in a separate run after replacing the diamond crystal by a nickel foil. Secondary electrons are momentum analyzed in the tagging magnet and registered by plastic scintillators each defining an energy interval of 2 MeV width. Channel 1 corresponds to 800 MeV, channel 351 to 50 MeV.

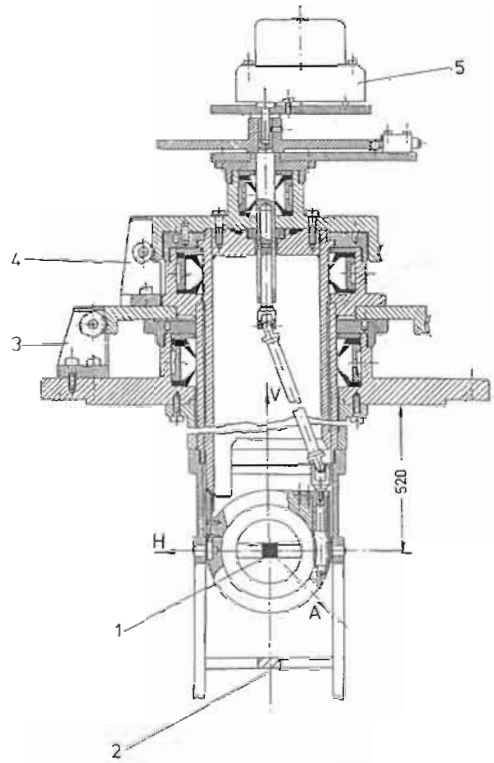

Fig. 2. Goniometer for the diamond crystal (1) and the comparison Ni radiator (2). The diamond crystal is mounted in the center of a circular holder with its [100] crystal axis parallel to the goniometer axis A. Three step-motor drives (3–5) may be used to rotate the holder around a vertical axis V, a horizontal axis H and an azimuthal axis A, the first two being parallel to the plane of the holder, the latter perpendicular to it. Axis V is fixed in space and carefully aligned perpendicular to the incoming electron beam. Axis H is fixed in the horizontal plane but its direction may be rotated by varying Φ_V. The direction of axis A is rotated in a vertical plane by varying Φ_H and its horizontal projection is rotated by varying Φ_V. By varying Φ_A the crystal holder is rotated without affecting the axes V and H. A DC-motor drive shifts the whole apparatus up and down in order to change the radiator.

In Eqs. (8) and (9) g_1, g_2 and g_3 are the components of g with respect to the normalized basis $(b_1/|b_1|, b_2/|b_2|, b_3/|b_3|)$. Maximum linear polarization is observed in the plane (g, p_0). Since the angle θ between b_1 and p_0 is small, we also may consider (g, b_1) as the plane of maximum linear polarization for the purposes of our present considerations. The angle difference $\beta = \varphi - \Phi_A$ fixes the plane of maximum linear polarization in a way that $\beta = 0$ means vertical and $\beta = \frac{\pi}{2}$ horizontal linear polarization. For the $g = [02\bar{2}]$ reciprocal lattice vector shown in Fig. 3 this means that

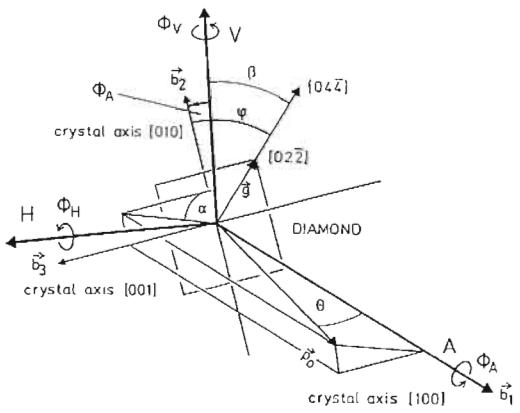

Fig. 3. Definition of the crystal angles (θ, α, φ) and goniometer angles (Φ_V, Φ_H, Φ_A). θ, α: polar angle and azimuth of the primary electron momentum p_0 in the $b_1 = [100]$, $b_2 = [010]$, $b_3 = [001]$ reference frame. φ: azimuth of the reciprocal lattice vector g responsible for the production of coherent bremsstrahlung in the same reference frame. The axis [100] is carefully aligned to coincide with A to better than 2 mrad. Φ_V, Φ_H and Φ_A: angles of rotation of the three goniometer axes V, H and A with respect to their respective zero-positions defined by the conditions (i) $\theta = 0$, (ii) b_2 parallel to the vertical direction V. β: angle between the plane of maximum polarization and the vertical direction V. $\beta = 0$: vertical polarization. $\beta = \frac{\pi}{2}$: horizontal polarization. Φ_V^0, Φ_H^0, Φ_A^0: random starting positions of the goniometer drives.

$\Phi_A = +45°$ leads to vertical and $\Phi_A = -45°$ to horizontal linear polarization.

The following relations are valid between the goniometer angles Φ_V, Φ_H and Φ_A and the crystal angles α, θ and φ:

$$\Phi_V = \arcsin(\sin\theta \sin(\alpha + \Phi_A)); \quad (10)$$

$$\Phi_H = -\arctan(\tan\theta \cos(\alpha + \Phi_A)); \quad (11)$$

$$\theta = \arccos(\cos\Phi_H \cos\Phi_V); \quad (12)$$

$$\alpha = \arccos\big([-\cos\Phi_A \sin\Phi_H \cos\Phi_V + \sin\Phi_A \sin\Phi_V][\sin\theta]^{-1}\big), \quad (13)$$

$$\varphi = \Phi_A + \beta. \quad (14)$$

One of the premises of the relations given above is that at the beginning of any rotation we have $\theta = 0$ and $\Phi_A = 0$. This means that the crystal axes [100], [010] and [001] coincide with the goniometer axes A, V and H, respectively, while being in their zero positions. The coincidence of the crystal axis [100] with the goniometer axis A has to be made better than 2 mrad in prealignment procedures. If this is not the case, characteristic irregularities will be observed in the intensity patterns. Such effects did not show up in the present experiment. We take this as a proof that the prealignement was very precise. When starting the rotation of the goniometer drives from a random position the angles Φ_V, Φ_H and Φ_A are not known with the desired precision, because optical alignments are not sufficiently precise to fix the zero points of these angles. The methods for a precise determination of these zero points are described in the next section.

4. Method of crystal orientation

When starting the rotation of the goniometer drives from a random position, the goniometer angles Φ_V, Φ_H and Φ_A are in general not zero but equal to unknown values of Φ_V^0, Φ_H^0 and Φ_A^0. These latter angles have to be determined in order to be able to make use of Eqs. (10) to (14). For the purpose of a determination of the angles Φ_V^0, Φ_H^0 and Φ_A^0 a collection of intensity patterns has been generated by computer simulation, so that by comparison of experimental and theoretical patterns information may be obtained on these angles of interest. These computer simulations take into account multiple scattering in a crystal of 0.1 mm thickness, a beam divergence of 0.2 mrad and reciprocal lattice vectors with Miller indices $0 \leqslant |h| \leqslant 2$, and $0 \leqslant |k|, |l| \leqslant 20$. The influence of the Debye–Waller factor has also been taken into account, which amounts to about 97% for the [02$\bar{2}$] reciprocal lattice vector and its analogues and decreases with increasing Miller indices. These parameters of the computer simulations reflect the actual experimental situation which is described in more detail in sections 6 and 7. Characteristic examples of the results obtained are shown in Figs. 4a–4e for rotations around the axis V as an example. Similar results are obtained for rotations around the axis H.

Fig. 4a corresponds to the case $\Phi_H^0 = \Phi_A^0 = 0$. In this figure the rotation around the V axis in the angular range -100 mrad $\leqslant \Phi_V \leqslant 100$ mrad corresponds to a variation of the crystal angle $\theta = |\Phi_V|$, with $\alpha = 270°$ for $\Phi_V \leqslant 0$ and otherwise $\alpha = 90°$ (see Eq. (10)). The intensity pattern is completely symmetrical around $\Phi_V = 0$ and this may be considered as a characteristic for a perfect prealignment of the crystal. All of the ridges in the intensity patterns correspond to more than one reciprocal lattice vector. Since in general the contributions of different reciprocal lattice vectors have different directions of maximum linear polarization this case is favourable for the intensity but unfavourable for the degree of linear polarization. By rotating around the axis H we would obtain an identical spectrum. For nonzero values of Φ_H^0 and Φ_A^0 the ridges seen in Fig. 4a split up into a larger number with part of them containing contributions from only one single reciprocal lattice vector.

Fig. 4b shows a typical case which may be observed when starting with a random setting of the goniometer angles after having carried out a good prealignment of the crystal axes. The figure is for the case of $\Phi_A^0 = 50$ mrad and $\Phi_H^0 = 10$ mrad, i.e. both of these angles are non-zero but small. This intensity pattern is nearly symmetrical around $\Phi_V = 0$. The pronounced discontinuity deviating strongly from symmetry with respect to $\Phi_V = 0$ belongs to the reciprocal lattice vector $[00\bar{4}]$. This unwanted discontinuity can be shifted out of the energy range of interest by increasing Φ_H. Details of this procedure will be discussed in the next section by making use of Fig. 7.

For the determination of the zero positions of the crystal angles from the intensity pattern it is of importance that the deviation of Φ_A^0 from zero is not too large at the beginning of an experiment. This unfavourable situation of a large Φ_A^0 is demonstrated in Fig. 4c. In this case we do not even have an approximate symmetry around $\Phi_V = 0$, leading to a very tedious alignment procedure. In this case it is difficult to find a connection between the intensities and the corresponding reciprocal lattice vectors. Therefore, this case should be avoided by means of a proper prealignment.

Fig. 5a shows an experimental intensity pattern versus photon energy E_γ and goniometer angle Φ_V for nonzero Φ_A^0 and Φ_H^0. By comparison with the calculated intensity patterns of Figs. 4b and 4c we see that Φ_A^0 must be somewhere between 50 mrad and 0.5 rad. The spectrum in Fig. 5a has no symmetry point on the Φ_V axis at $\Phi_V = 0$ as expected for small values Φ_A^0 (see Figs. 4a and 4b). By varying Φ_A^0, spectra with symmetry points may be found. At the end of these alignment procedures intensity patterns of the kind shown in Fig. 5b may be observed. For the fine tuning, contour plots as shown in Fig. 5c are favourable. From this figure it is easy to find the precise symmetry point corresponding to $\Phi_V = 0$. The method of finding $\Phi_H = 0$ is completely analogous to the case of finding $\Phi_V = 0$ described above.

Figs. 6a–6d show calculated and experimental intensity patterns versus photon energy E_γ and goniometer angle Φ_A, for fixed values of $\Phi_H^0 = 66.28$ mrad and $\Phi_V^0 = 0$. These settings of Φ_H and Φ_V are of interest in connection with the generation of linear polarization due to the reciprocal lattice vectors $g = [0 \pm 2 \pm 2]$, discussed in Fig. 7. The ridges contained in Fig. 6a are due to these reciprocal lattice vectors only. Fig. 6b contains also the ridges due to the reciprocal lattice vector $g = [0 \pm 4 \pm 4]$ which are the next prominent ones, and Fig. 6c the ridges due to Miller indices up to 20. The symmetry properties of these intensity patterns may be used to find the zero point of Φ_A in the alignment procedure of the crystal. Fig. 6d shows the experimental intensity pattern for the same goniometer settings as used for the calculated ones of Figs. 6a–6c. We see that the experimental pattern and the calculated pattern of Fig. 6c resemble each other in very detail, giving us confidence that the calculation is very precise. More quantitative information on the agreement between theory and experiment is given in Fig. 11a.

5. Selection of reciprocal lattice vectors favourable for linear polarization

The purpose of this section is to explore how the intensity patterns are composed of contributions from different reciprocal lattice vectors and how these contributions can be identified in experimental results. This point is of special importance for the generation of high degrees of linear polarization because for this purpose it is necessary to isolate one of the reciprocal lattice vectors $g = [0 \pm 2 \pm 2]$, which are the most favourable ones. Fig. 6a shows the calculated intensity pattern due to these reciprocal lattice vectors only. When including more reciprocal lattice vectors into the calculation as done in Figs. 6b–6c the intensity pattern becomes more complex but the contributions of $[0 \pm 2 \pm 2]$ remain the most prominent ones and still are easily identifiable. The calculated pattern of Fig. 6c is already in very close agreement with the experimental pattern of Fig. 6d. This close agreement makes it easy to identify the $[0 \pm 2 \pm 2]$ contributions also in the experimental pattern.

In Figs. 7a–7e we describe the procedure by which horizontal linear polarization may be obtained by making use of the $[02\bar{2}]$ reciprocal lattice vector. After a rotation of the crystal by $\Phi_A = -45°$ out of its zero position the reciprocal lattice vectors [022] and $[0\bar{2}\bar{2}]$ are directed vertically and the reciprocal lattice vectors $[02\bar{2}]$ and $[0\bar{2}2]$ are parallel to the goniometer axis H. This case is described in Fig. 7, where 7a shows the crystal position viewed in direction of the goniometer axis A and 7b the crystal position viewed in direction of the goniometer axis H. In Fig. 7b the shaded area depicts the zone ("pancake") of momentum transfers contributing to coherent bremsstrahlung. It is apparent that all the reciprocal lattice vectors of small Miller indices are outside the pancake but very close to it. This unfavourable case has to be modified in a way that the $[02\bar{2}]$ reciprocal lattice vector is in the "pancake" and all the others which are not parallel to $[02\bar{2}]$ are far away from the pancake. This can be achieved by rotating around the H axis by $\Phi_H \approx 60$ mrad. This keeps the reciprocal lattice vectors $[02\bar{2}]$ and $[0\bar{2}2]$ which are parallel to each other on the H axis and close to the "pancake", whereas the [022] and the $[0\bar{2}\bar{2}]$ vectors and the vectors having higher Miller indices are shifted far outside the kinematical range of the "pan-

cake" (Figs. 7c and 7d). After rotating around the V axis of the goniometer by

$$\sin \Phi_V = -\frac{\delta}{\sqrt{k^2+l^2}\,\frac{2\pi}{a}}, \tag{15}$$

with k, $l = 2$, only the vector $g = [02\bar{2}]$ is at the lower kinematical border of the "pancake" and gives the highest contribution to the linearly polarized coherent bremsstrahlung. The single point spectrum obtained in this way has a very high degree of linear polarization and the polarization vector being in the (p_0, g) plane is horizontal. It is important to note that the precise angle Φ_H is not of importance. It only is important that Φ_H is large enough to separate the other reciprocal lattice vectors from the pancake, in a first place [040] and [00$\bar{4}$] which otherwise would contribute to the discontinuity and reduce the degree of linear polarization. The selection of one reciprocal lattice point to give linear polarization in the horizontal direction described above is not the only possibility as can easily be deduced with the help of considerations similar to those of Figs. 7a to 7e.

Analogous considerations lead to the conditions for maximum linear polarization in the vertical direction, keeping the angle $\Phi_A = -45°$ unmodified and using the reciprocal lattice vector [022]. In this case, however, we have to take into consideration that any rotation around V rotates also the direction of H within the horizontal plane. This increases the required rotation around H by a factor $1/\cos \Phi_V$, leading to

$$\sin \Phi_H = \frac{\delta}{\cos \Phi_V \sqrt{k^2+l^2}\,\frac{2\pi}{a}}. \tag{16}$$

In this orientation the polarization vector is vertical for $\Phi_V \approx 60$ mrad.

Summarizing we can say that photon spectra with a high degree of linear polarization can be generated in the following way:

– make the crystal angles $\theta = \alpha = \varphi = 0$, which is the same as finding Φ_V^0, Φ_H^0 and Φ_A^0;

– rotate around the A axis by $\Phi_A = -45°$ (or by $+45°$);

– for horizontal polarization rotate around the H axis by $\Phi_H \approx 60$ mrad and rotate around the V axis in accordance with Eq. (15);

– for vertical polarization rotate around the V axis by $\Phi_V \approx 60$ mrad and rotate around the H axis in accordance with Eq. (16).

For practical applications the results of this paragraph are summarized in Table 1 (see Fig. 8 for a typical one-point spectrum obtained in this way). Angle θ was always chosen to be 60 mrad. Smaller values for θ slightly decrease the degree of linear polarization because of insufficient separation of reciprocal lattice vectors with larger Miller indices whereas larger values of θ lead to only marginal increases.

6. Influence of beam divergence and multiple scattering on coherent bremsstrahlung

In addition to the known Debye–Waller factor, realistic predictions of intensities and degrees of linear polarization of coherent bremsstrahlung have to include the following effects:

- multiple scattering of electrons in the crystal;
- divergence of the electron beam;
- possible mosaic structure of the diamond crystal;
- energy uncertainty of the electron beam.

The energy uncertainty of MAMI is small (≈ 150 keV), so that the influence of this uncertainty is small in comparison to that of beam divergence and multiple scattering.

For taking into account the beam divergence we assume that the angular dependence of electron directions follows a Gaussian distribution with a variance σ^2_{beam}. This quantity is composed of a horizontal and a vertical part which are known to be somewhat different. For the present purpose, however, we only fit one parameter, which may be considered as an effective average over the two contributions. Summarizing, we may write

$$P(\theta_h)\,\mathrm{d}\theta_h = \frac{1}{\sqrt{2\pi}\,\sigma_h}\exp\left(-\frac{1}{2}\frac{\theta_h^2}{\sigma_h^2}\right)\mathrm{d}\theta_h, \tag{17}$$

$$P(\theta_v)\,\mathrm{d}\theta_v = \frac{1}{\sqrt{2\pi}\,\sigma_v}\exp\left(-\frac{1}{2}\frac{\theta_v^2}{\sigma_v^2}\right)\mathrm{d}\theta_v, \tag{18}$$

and

$$P(\theta_b)\,\mathrm{d}\Omega_b = \frac{1}{\pi\sigma^2_{\text{beam}}}\exp\left(-\frac{\theta_b^2}{\sigma^2_{\text{beam}}}\right)2\pi\theta_b\,\mathrm{d}\theta_b, \tag{19}$$

where $\theta_b = \sqrt{\theta_h^2+\theta_v^2}$ is the polar angle and $\mathrm{d}\Omega_b$ the solid-angle element for the incoming electron beam. For the present case of axial symmetry the variances $\sigma_h^2 = \langle\theta_h^2\rangle$, $\sigma_v^2 = \langle\theta_v^2\rangle$ and $\sigma^2_{\text{beam}} = \langle\theta_b^2\rangle$ are related to each other via the equation $\sigma^2_{\text{beam}} = 2\sigma_h^2 = 2\sigma_v^2$.

Multiple scattering of electrons on their pass through the crystal leads to a further increase of the beam divergence. The basis of our calculation is Moliere's theory of multiple scattering [23]. The probability of finding an electron in the solid-angle interval $\mathrm{d}\Omega_s$ located between the polar angles θ_s and $\theta_s + \mathrm{d}\theta_s$ is given by

$$P(\theta_s)\,\mathrm{d}\Omega_s = \frac{1}{\pi\sigma^2_{\text{mol}}}\exp\frac{-\theta_s^2}{\sigma^2_{\text{mol}}}2\pi\theta_s\,\mathrm{d}\theta_s. \tag{20}$$

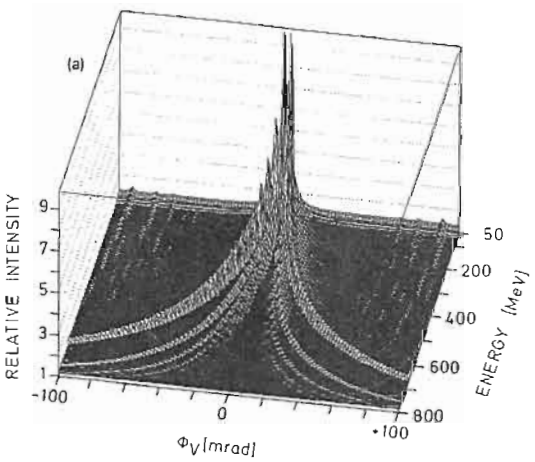

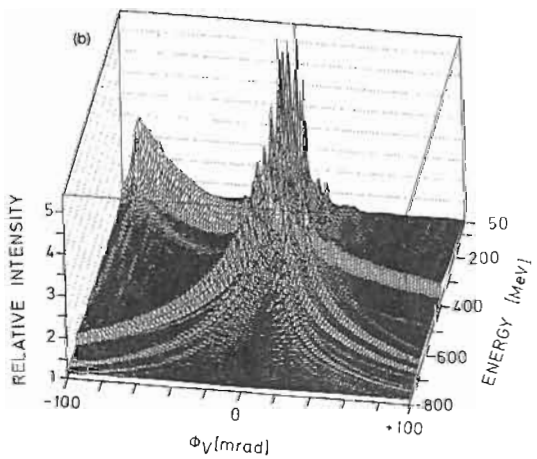

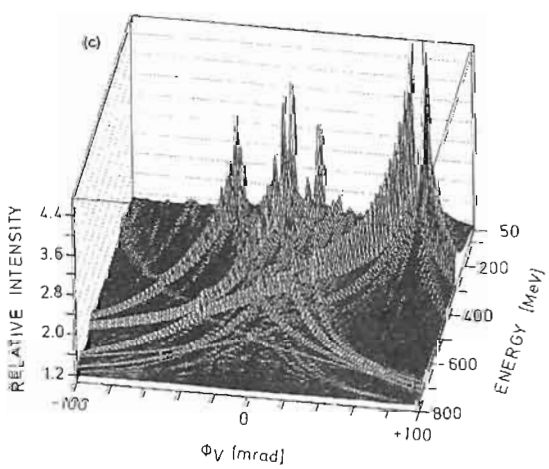

Moliere's theory of multiple scattering allows a calculation of the standard deviation $\sigma_{\text{mol}} = \langle \theta_s^2 \rangle^{1/2}$ which is given by

$$\sigma_{\text{mol}} = \theta_1 (B - 1.2)^{\frac{1}{2}}, \tag{21}$$

$$\theta_1^2 = (0.157\ \text{MeV}^2\ \text{cm}^2) \frac{Z(Z+1)}{A} \frac{t}{p^2 v^2}, \tag{22}$$

where p is the momentum and v the velocity of the electron. The quantity Z is the charge number, A the mass of 1 mol in [g] and t the thickness of the layer in [g/cm^2]. The dimension of the product pv is [MeV]. The quantity B is given by

$$B - \ln B = b, \tag{23}$$

with b given by

$$b = \ln \Omega_b + 1 - 2C, \tag{24}$$

with $C = 0.577\cdots$ being Euler's constant and Ω_b the number of collisions. This latter quantity is given by

$$\Omega_b = (7800\ \text{cm}^2) \frac{(Z+1) Z^{\frac{1}{3}} t}{\beta^2 A (1 + 3.35\alpha^2)}, \tag{25}$$

where $\beta = v/c$ and $\alpha = zZ/137\beta$.

Since multiple scattering of electrons in the diamond crystal leads to a gradual increase of the beam divergence, we use an appropriate average $\sigma_{\text{scatt}} = \overline{\sigma_{\text{mol}}}$ over the path length of the quantity σ_{mol} defined in Eq. (21) for the calculation to follow. Then the resulting effective angular distribution of electrons contributing to coherent bremsstrahlung is given by

$$P(\theta)\, \mathrm{d}\Omega = \frac{1}{\pi \sigma_{\text{tot}}^2} \mathrm{e}^{-(\theta^2/\sigma_{\text{tot}}^2)} 2\pi\theta\, \mathrm{d}\theta, \tag{26}$$

Fig. 4. (a) Relative intensity $I^{\text{rel}} = (I^{\text{coh}} + I^{\text{incoh}})/I^{\text{incoh}}$ of coherent bremsstrahlung versus photon energy E_γ calculated for a diamond crystal of a thickness of 0.1 mm, including the effects of divergence of the incoming beam of $\sigma_{\text{beam}} = 0.2$ mrad and including multiple scattering of the electrons in the crystal of 100 μm thickness. Reciprocal lattice vectors with $0 \leqslant |h| \leqslant 2$ and $0 \leqslant |k|, |l| \leqslant 20$ are taken into account. Goniometer angles: $\Phi_H^0 = \Phi_A^0 = 0$ fixed, Φ_V variable. The comparitively small number of ridges contain contributions from more than one reciprocal lattice vectors g. (b) Same as (a) but for fixed $\Phi_A^0 = 50$ mrad and $\Phi_H^0 = 10$ mrad. Since both angles Φ_A^0 and Φ_H^0 are non-zero but small, this pattern represents the general case of an intensity pattern to start with in finding the exact zero positions of the goniometer after a good prealignment of the crystal. (c) Same as (a), but for fixed $\Phi_A^0 = 0.5$ rad and $\Phi_H^0 = 20$ mrad. Because of the large Φ_A^0 this pattern may be considered typical for a bad prealignment of the crystal. This pattern strongly deviates from symmetry around $\Phi_V = 0$ and makes the precise determination of the zero position of the goniometer difficult.

with

$$\sigma_{tot} = \sqrt{\sigma_{beam}^2 + \sigma_{scatt}^2}\,. \tag{27}$$

The contributions of crystal thickness or σ_{mol} on the one hand and the divergence σ_{beam} of the incoming electron beam on the other are depicted in Figs. 9 and 10. The use of $\sigma_{scatt} = \overline{\sigma_{mol}}$ proposed here is an approximation which may be replaced by a more refined procedure where the diamond crystal is subdivided into separate layers and the predictions of intensities and degrees of linear polarization are made for each layer separately. However, for the present cases the two ways of calculation led to the same result.

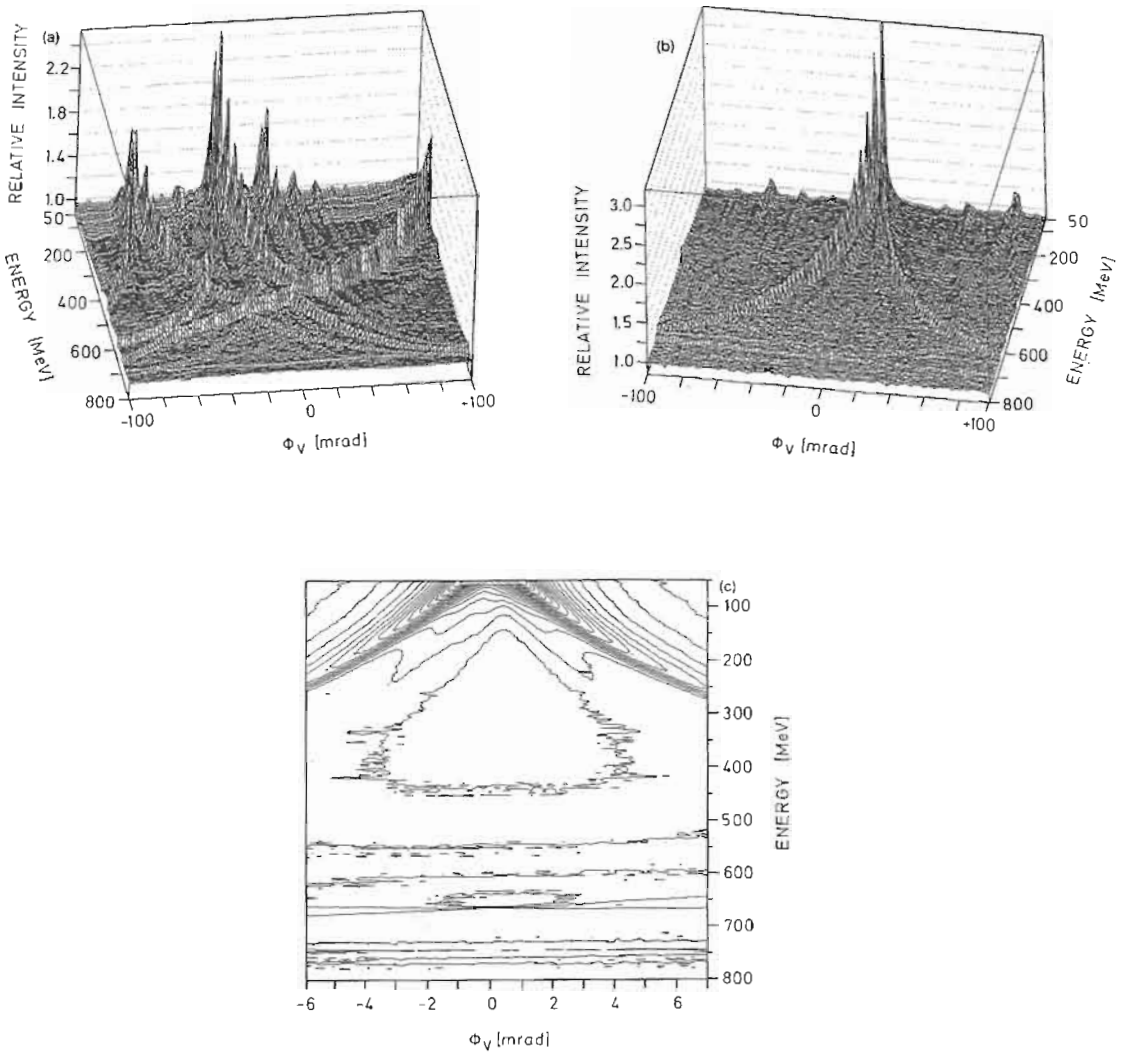

Fig. 5. (a) Experimental relative intensity $I^{rel} = (I^{coh} + I^{incoh})/I_{Ni}^{incoh}$ versus photon energy E_γ and goniometer angle Φ_V for non-zero values of Φ_H^0 and Φ_A^0 measured at the beginning of the alignment procedure. Variations of the intensity of the electron beam are eliminated by normalizing the energy spectra to give constant intensity at the high energy end of the spectrum where the coherent spectrum is almost independent of the crystal angles. (b) Same as in (a) but measured at the end of the alignment procedure. (c) Experimental relative intensity $I^{rel} = (I^{coh} + I^{incoh})/I_{Ni}^{incoh}$ as a high angular resolution contour diagram versus photon energy E_γ and goniometer angle Φ_V for small non-zero values of Φ_H^0 and Φ_A^0. This type of data representation is favourable for the determination of the symmetry point on the Φ_V scale. Analogous diagrams may be used to find also the symmetry points on the Φ_H and Φ_A scales.

7. Comparison of calculated and experimental intensities of coherent bremsstrahlung

The purpose of this section is to explore to what extent calculated and experimental relative intensities agree with each other. Simultaneously, the beam divergence will be determined which is the only free parameter of the calculation. The temperature is choosen to be 293 K.

The comparison of experimental and theoretical relative intensities is carried out in Fig. 11a where the peak of intensities due to the [02$\bar{2}$] reciprocal lattice vector is located in the energy region of the Δ resonance. The intensity patterns shown in the foregoing sections have been obtained by dividing the intensities measured with the diamond radiator by the corresponding intensities measured with the Ni radiator. This method is sufficient for determining the crystal orientation, but is not accurate enough for the present purpose of a detailed comparison between experimental and calculated intensities. The reason is that the incoherent spectra depend on the charge number Z of the radiator.

For the calculation of incoherent bremsstrahlung

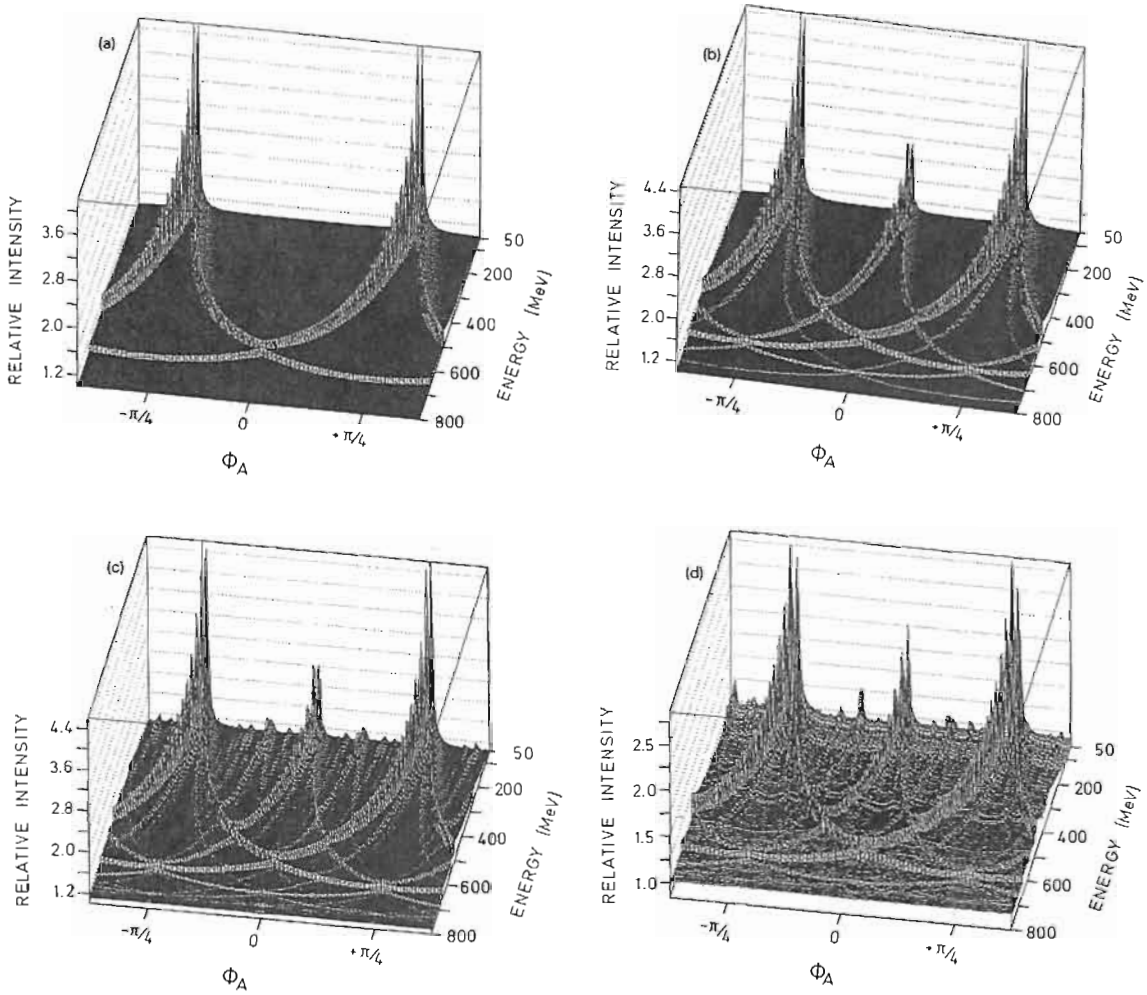

Fig. 6. (a) Calculated relative intensity $I^{rel} = (I^{coh} + I^{incoh})/I^{incoh}$ versus photon energy E_γ and goniometer angle Φ_A. $\Phi_H^0 = 66.28$ mrad, $\Phi_V^0 = 0$. Properties of beam and crystal are the same as in Fig. 4a. Coherent bremsstrahlung is assumed to be due to the reciprocal lattice vectors $g = [0 \pm 2 \pm 2]$ only. (b) Same as (a) but for reciprocal lattice vectors up to $g = [0 \pm 4 \pm 4]$. (c) Same as (a) but for Miller indices up to 20. (d) Experimental relative intensity $I^{rel} = (I^{coh} + I^{incoh})/I_{Ni}^{incoh}$ versus photon energy E_γ and goniometer angle Φ_A. $\Phi_H^0 = 66.28$ mrad, $\Phi_V^0 = 0$. Note that the goniometer angles are the same as assumed in (a)–(c).

from C and Ni we follow the prescriptions of Timm [19] and Diambrini [18] but use the atomic structure factor of Cromer and Waber [24] based on self consistent wavefunctions, instead of estimates based on the Thomas–Fermi model. The resulting correction factor deviates from 1 by less than $\pm 2\%$ at energies below $x = 0.8$ if we normalize the intensity spectra to give the same energy-integrated average. At the high energy end of the spectrum at $x = 0.8$, however, the correction factor deviates from 1 by up to 5% and, therefore, has to be included in order to obtain satisfactory agreement between experiment and prediction.

The agreement between experimental and calculated relative intensities shown in Fig. 11a is excellent, where an effective beam divergence of $\sigma_{\text{beam}} = 0.2$ mrad has been used for the calculation. This gives us confidence that predictions for the degrees of linear polarization

$$P = \frac{I_{\parallel} - I_{\perp}}{I_{\parallel} + I_{\perp}}, \tag{28}$$

made on the same basis as the predictions for the intensities are also very precise. The degrees of linear polarization corresponding to the intensities of Fig. 11a are shown in Fig. 11b.

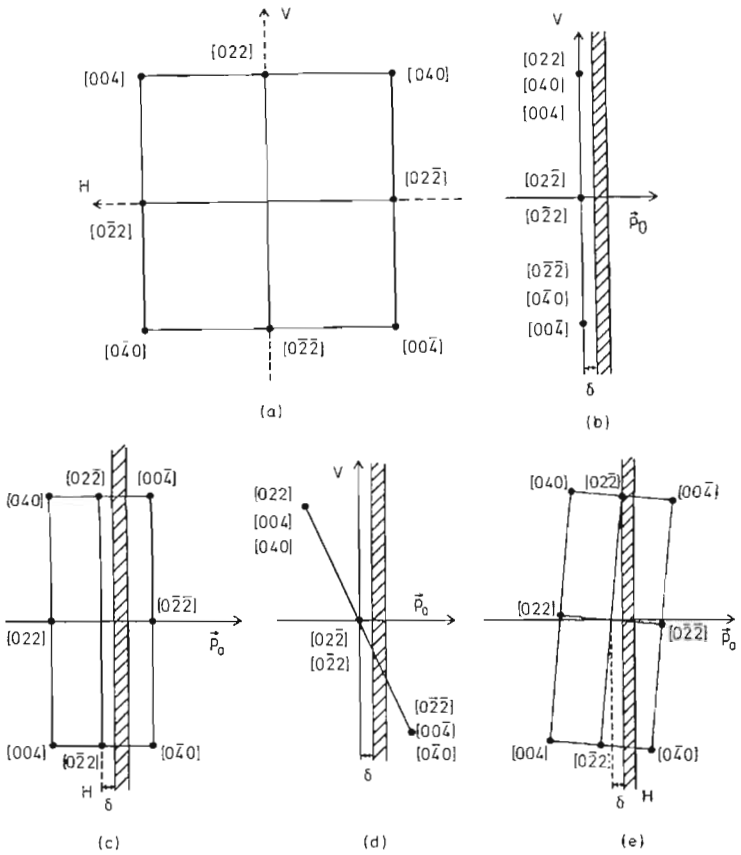

Fig. 7. Orientation of the reciprocal lattice vector in the laboratory frame after rotating the A axis by $\Phi_A = -45°$ with respect to its zero position and keeping $\Phi_V = \Phi_H = 0$ constant. (a) View on the diamond crystal from a direction opposite to the electron beam. (b) Same as (a) but view from a direction opposite to the H axis. This figure also shows the "pancake" between the lower kinematical border $\delta(x)$ for a given x and $2\delta(x)$. (c–e): Orientation of the reciprocal lattice vector in the laboratory frame after rotating the A axis by $\Phi_A = -45°$, keeping $\Phi_V = 0$ constant and rotating $\Phi_H \approx 60$ mrad (not to scale). (c) Reciprocal lattice vectors when viewing from a direction opposite to the V axis. (d) View from a direction opposite to the H axis. (e) Final position after rotating also around the V axis by a very small angle Φ_V. This latter view is from a direction opposite to the V axis. It is important to notice that from all the reciprocal lattice vectors only [02$\bar{2}$] is on the kinematical border δ and, therefore, makes the strongest possible contributes to coherent bremsstrahlung.

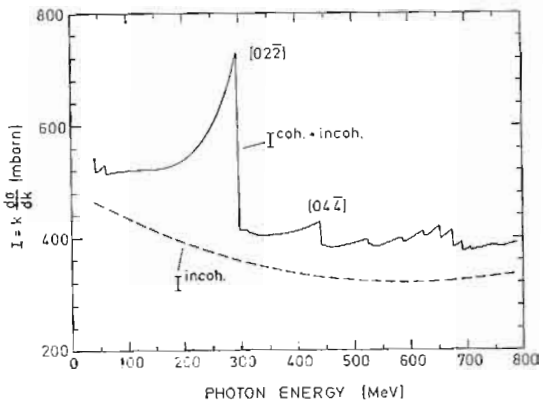

Fig. 8. Typical one-point spectrum: intensity $I = k(\mathrm{d}\sigma\ \mathrm{d}k)$ as a function of photon energy E_γ calculated for $\theta = 60°$ and $\alpha = 0.6452$ rad. The first discontinuity is solely due to the reciprocal lattice vector [02$\bar{2}$], the second due to [04$\bar{4}$].

8. Degrees of linear polarization to be achieved at MAMI with collimated photon beams

The high quality of the MAMI electron beam allows a collimation of the photon beam without collimating the incident electron beam. It is reasonable to assume that a collimation angle (half opening angle) of up to $\theta_c = \frac{1}{2}\theta_\gamma$ may be achieved where $\theta_\gamma = 0.6$ mrad is the characteristic angle of the bremsstrahlung beam. Smaller collimation angles are not impossible but re-

Table 1
Recommended crystal orientations for the production of single point spectra with high degree of linear polarization due to the reciprocal lattice vector [02$\bar{2}$] for horizontal linear polarization and [022] for vertical polarization. Angles are measured in rad. Electron energy $E_0 = 855$ MeV. For each energy the first line corresponds to vertical and the second line to horizontal linear polarization. The azimuthal angle is $\Phi_A = -45°$, the polar angle $\theta = 60$ mrad

E_γ [MeV]	α	Φ_V	Φ_H
100	0.7511	0.0600	−0.0021
100	0.7511	−0.0021	−0.0600
150	0.7303	0.0599	−0.0033
150	0.7303	−0.0033	−0.0599
200	0.7063	0.0598	−0.0048
200	0.7063	−0.0047	−0.0598
250	0.6782	0.0597	−0.0064
250	0.6782	−0.0064	−0.0597
300	0.6450	0.0594	−0.0084
300	0.6450	−0.0083	−0.0594
350	0.6050	0.0590	−0.0108
350	0.6050	−0.0108	−0.0590
400	0.5558	0.0584	−0.0137
400	0.5558	−0.0137	−00584
450	0.4936	0.0575	−0.0173
450	0.4936	−0.0173	−0.0575
500	0.4122	0.0559	−0.0219
500	0.4122	−0.0219	−0.0559
550	0.2997	0.0531	−0.0280
550	0.2997	−0.0280	−0.0531
600	0.1305	0.0476	−0.0366
600	0.1305	−0.0365	−0.0476

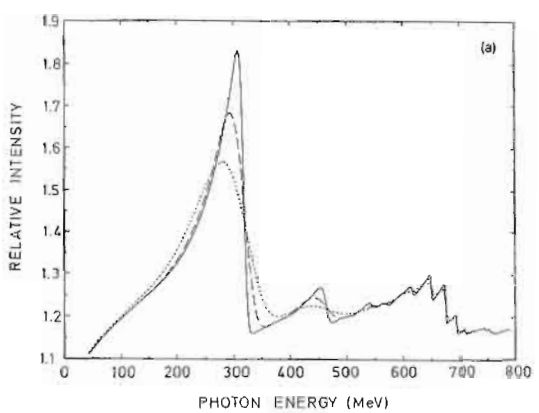

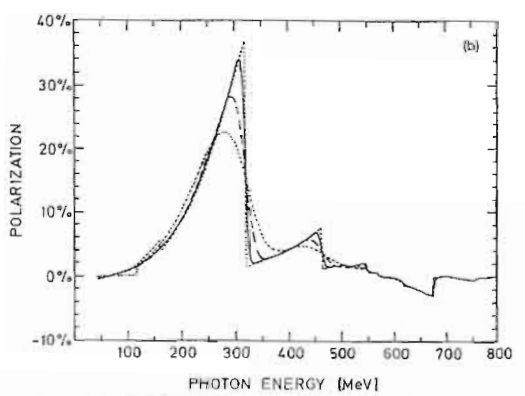

Fig. 9. (a) Calculated influence of beam divergence and multiple scattering on the relative intensity $I^{rel} = (I^{coh} + I^{incoh})/I^{incoh}$ of coherent bremsstrahlung. $E_0 = 855$ MeV, $\theta = 60$ mrad, $\alpha = 0.63$ rad. Crystal thickness 0.1 mm, beam divergences $\sigma_{beam} = 0.2$ mrad (full line), 1 mrad (dashed line), 2 mrad (dotted line). (b) Calculated influence of multiple scattering and beam divergence on the degree of linear polarization. $E_0 = 855$ MeV, $\theta = 60$ mrad, $\alpha = 0.63$ mrad, crystal thickness 0.1 mm. Beam divergences: $\sigma_{beam} = 0.1$ mrad (full line), 1 mrad (dashed line), 2 mrad (dotted line). The additional dotted line shows the case of $\sigma_{beam} = 0$ and crystal thickness tending to zero.

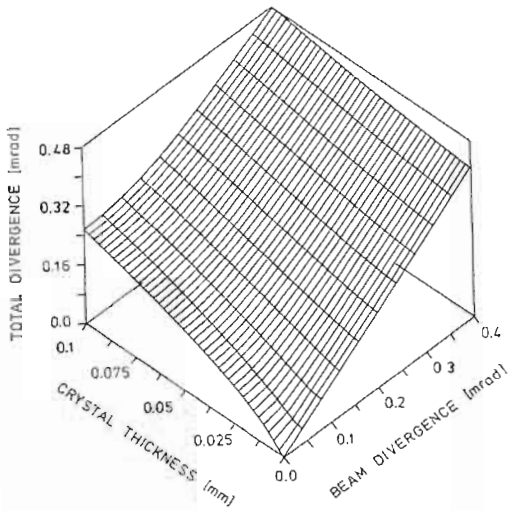

Fig. 10. Contributions of beam divergence and multiple scattering to the total divergence of the distribution of electron directions in the diamond crystal. The divergences are defined as the variances σ^2 of Gaussian distributions, as defined in Eqs. (19) and (27). The standard deviation corresponding to multiple scattering σ_{scatt} is the average over the length of the crystal. The standard deviation σ_{beam} of the beam divergence is an effective quantity averaging over the horizontal and vertical parts. The total divergence σ_{tot} is the pythagorean sum of the two partial divergences.

quire major improvements in the handling of the electron beam.

In Figs. 12a and 12b we explore the influence of beam collimation on the relative intensity of coherent bremsstrahlung and on the degree of linear polarization, respectively. In the calculation the thickness of the crystal was assumed to be the same as used in our present experiment, i.e. 0.1 mm. For the beam divergence we used $\sigma_{\text{beam}} = 0.2$ mrad which was determined by comparison of the measured and predicted relative intensities as described in section 7. The peaks correspond to the reciprocal lattice vector $[02\bar{2}]$. The discontinuities at $E_\gamma^{\text{d}} = 320$ MeV correspond to the exact forward direction of the coherent bremsstrahlung beam. Collimating the beam introduces a lower cut-off energy E_γ^{c} into the two spectra being at about 280 MeV for a collimator of $\theta_{\text{c}} = 0.3$ mrad. The collimator reduces the incoherent part of the spectra but leaves the coherent spectrum of the reciprocal lattice vector $[02\bar{2}]$ between E_γ^{c} and E_γ^{d} unmodified. Due to this effect the relative intensity as well as the degree of linear polarization P are increased in this energy interval. In our example P is about 50% at the cut-off energy E_γ^{c} and 56% at the discontinuity E_γ^{d}, leading to an average of 53%.

For the calculations leading to Figs. 12a and 12b we made use of the fact that the angular distribution of incoherent bremsstrahlung with respect to the direction of the incoming electron may be represented with very good precision by the superposition of two Gaussian distributions

$$P(\theta_k)\,\mathrm{d}\Omega_k = \frac{1}{\pi \sum_{i=1}^{2} A_i \sigma_i^2} \times \sum_{i=1}^{2} A_i\, \mathrm{e}^{-(\theta_k/\sigma_i)^2} 2\pi\theta_k\,\mathrm{d}\theta_k, \qquad (29)$$

where $A_1 = 0.70$, $A_2 = 0.30$, $\sigma_1 = 0.383$ mrad and $\sigma_2 = 0.846$ mrad. Making use of the additivity of variances,

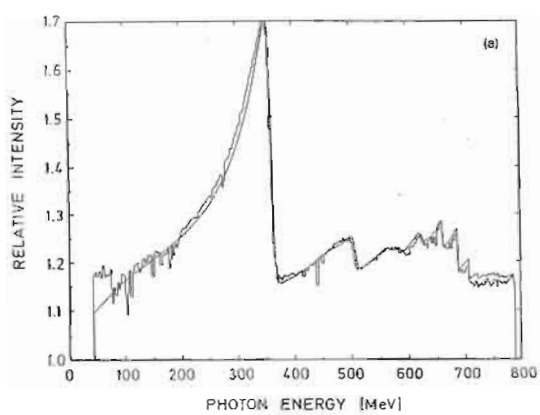

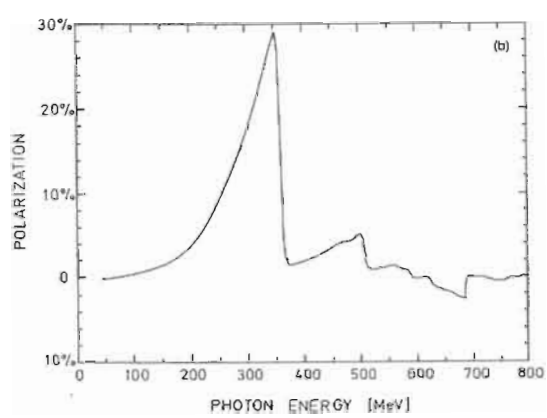

Fig. 11. (a) Relative intensity $(I^{\text{coh}} + I^{\text{incoh}})/I^{\text{incoh}}$ of coherent bremsstrahlung versus photon energy. $\theta = 66.28$ mrad, $\alpha = 0.61170$ rad, $E_0 = 855$ MeV, beam divergence $\sigma_{\text{beam}} = 0.2$ mrad. Histogram: experimental result. Continuous curve: result of calculation. (b) Predicted degree of linear polarization corresponding to the intensity spectrum of (a).

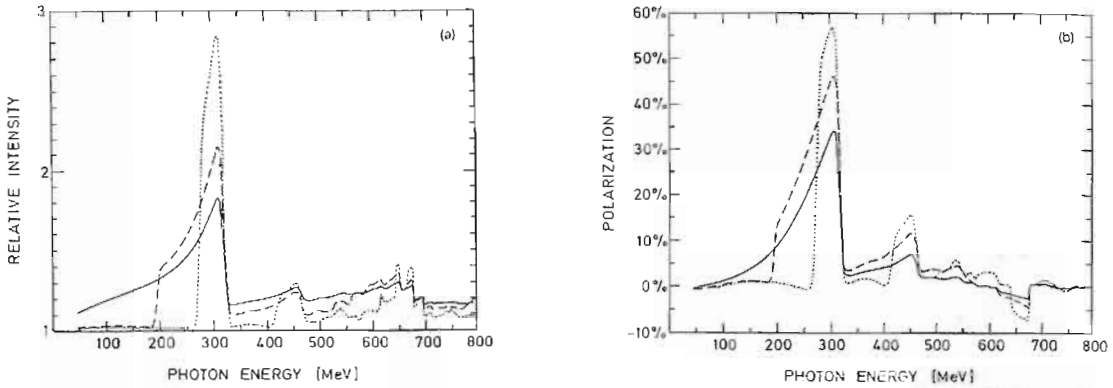

Fig. 12. (a) Estimated relative Intensity $I^{rel} = (I^{coh} + I^{incoh})/I^{incoh}$ as a function of photon energy for different collimations of the beam. $E_0 = 855$ MeV, beam divergence $\sigma_{beam} = 0.2$ mrad, crystal thickness 0.1 mm, $\theta = 60$ mrad, $\alpha = 0.63$ rad. Without collimation (solid line), $\theta_c = \theta_\gamma = 0.6$ mrad (dashed line), $\theta_c = \frac{1}{2}\theta_\gamma = 0.3$ mrad (dotted line). (b) Estimated degree of linear polarization for a crystal angle of $\varphi = \pi/4$, corresponding to maximum linear polarization from the [02$\bar{2}$] reciprocal lattice vector. The curves are calculated assuming approximately the same conditions as used for the corresponding curves in Fig. 11a.

the angular distribution of incoherent bremsstrahlung including the angular divergence of the incoming electron beam and multiple scattering can be represented in a simple closed form, which also allows an easy calculation of the reduction of incoherent bremsstrahlung due to collimation. This procedure is very precise for predicting the effects of collimation on the incoherent part of the bremsstrahlung. On the other hand the effects of collimation on the coherent part are taken into account only in an approximative way, where the approximations become effective only for non-zero σ_{beam} and non-zero σ_{scatt} defined in section 6. In this approximation we take into account the distribution of orientations of the incident electrons in the crystal in an exact way but disregard the fact that photons emitted parallel to p_0 do not enter the collimator parallel to its axis when p_0 is not parallel to this axis.

For a further improvement on the degree of linear polarization P it is necessary to reduce the beam divergence and the thickness of the crystal. The maximum degree of polarization to be achieved with an ideal electron beam, i.e. $\sigma_{beam} = \sigma_{scatt} = 0$, is shown in Fig. 13 for different collimators. It appears to be a reasonable assumption that the practical upper limit for the degree of linear polarization is located somewhere between curves b and c. This leads to estimates of the degrees of linear polarization of 80% at 200 MeV, 65% at 300 MeV, 55% at 400 MeV and 35% at 500 MeV.

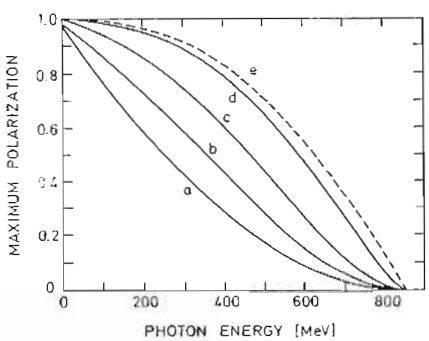

Fig. 13. Predicted highest degree of linear polarization obtainable for different half opening-angles θ_c of the collimator, using $\sigma_{beam} = \sigma_{scatt} = 0$: electron energy $E_e = 855$ MeV, reciprocal lattice vector $g = [0 \pm 2 \pm 2]$. (a) $\theta_0 = \infty$, (b) $\theta_c = 0.6$ mrad, $\theta_c = 0.3$ mrad, (d) $\theta_c = 0.1$ mrad, (e) degree of linear polarization after complete removal of incoherent bremsstrahlung.

References

[1] C.E. Thorn, G. Giordano, O.C. Kistner, G. Matone, A.M. Sandorfi and C.S. Whisnant, Nucl. Instr. and Meth. A 285 (1989) 447.

[2] G.S. Blanpied, M. Blecher, A. Caracappa, C. Djalali, A.-M. Duval, G. Giordano, S. Hoblit, O.C. Kistner, G. Matone, L. Miceli, W.K. Mize, B.M. Preedom, A.M. Sandorfi, C. Schaerf, R.M. Sealock, C.E. Thorn, S.T. Thornton, K. Vaziri and C.S. Whisnant, Phys. Rev Lett. 67 (1991) 1206.

[3] G. Blanpied, M. Blecher, A. Caracappa, C. Djalali, M.-A. Duval, G. Giordano, S. Hoblit, M. Khandaker, O.C. Kistner, G. Matone, L. Miceli, W.K. Mize, B.M. Preedom, A.M. Sandorfi, C. Schaerf, R.M. Sealock, C.E. Thorn, S.T. Thornton, K. Vaziri, C.S. Whisnant, X. Zhao and M.A. Moinester, preprint.

[4] F.H. Dyson and H. Überall, Phys. Rev. 99 (1955) 604.

[5] H. Überall, Phys. Rev. 103 (1956) 1055.

[6] H. Überall, Phys. Rev. 107 (1957) 223.
[7] H. Überall, Z. Naturforsch. 17a (1962) 332.
[8] G. Bologna, G. Diambrini and D.P. Murtas, Phys. Rev. Lett. 4 (1969) 134; ibid. 572;
G. Barbiellini, G. Bologna, G. Diambrini and G.P. Murtas, Phys. Rev. Lett. 8 (1962) 112; ibid. 454; ibid. 9 (1962) 396.
[9] S. Kato, T. Kifune, Y Kimura, M. Kobayashi, K. Kondo, T. Nishikawa, H. Sasaki, S. Kikuta and K. Kohra, J. Phys. Soc. Jpn 20 (1965) 303;
T Kifune, Y. Kimura, M. Kobayashi, K. Kondo and T. Nishikawa, J. Phys. Soc. Jpn 21 (1966) 1905.
[10] G. Bologna, G. Lutz, H.D. Schulz, U. Timm and W. Zimmermann, Nuovo Cimento 42 (1966) 844;
L. Criegee, G. Lutz, H.D. Schulz, U. Timm and W. Zimmermann, Phys. Rev. Lett. 16 (1966) 1031;
G. Lutz and U. Timm, Z. Naturforsch. 21a (1966) 1976.
[11] R.F. Mozley and J. De Wire, Nuovo Cimento 27 (1963) 1281.
[12] G. Bologna, Nuovo Cimento 49A (1967) 756.
[13] G. Lutz, Nuovo Cimento 53 (1968) 242.
[14] L. Criegee, M. Garrell, H. Sadrozinski, U. Timm and W. Zimmermann, Phys. Lett. 28B (1968) 140.
[15] H. Genzel, P. Joos and W. Pfeil, Landolt-Börnstein, Neue Serie, vol. 8 (1973) 1.
[16] D. Menze, W. Pfeil and R. Wilke, ZAED Physik Daten, Compilation of Pion Photoproduction Data, Zentralstelle für Atomkernenergie-Dokumentation, Eggenstein-Leopoldshafen, 1977.
[17] I. Arai and H. Fujü, Nucl. Phys. B 194 (1982) 251.
[18] G. Diambrini Palazzi, Rev. Mod. Phys. 40 (1968) 611.
[19] U. Timm, Fortschr. Phys. 17 (1969) 765.
[20] M.L. Ter-Mikaelian, High-Energy Electromagnetic Processes in Condensed Media (Wiley-Interscience, New York, 1972).
[21] A.W. Sáenz and H. Überall, Coherent Radiation Sources (Springer, Berlin, 1985).
[22] I. Anthony, J.D. Kellie, S.J. Hall, G.J. Miller and J. Ahrens, Nucl. Instr. and Meth. A 301 (1991) 230;
H. Herminghaus, A. Feder, K.H. Kaiser, W. Manz and H. v.d. Schmitt, Nucl. Instr. and Meth. 138 (1976) 1;
H. Herminghaus, Proc. 1970 Linear Acc. Conf., Albuquerque, NM, USA.
[23] G. Molière, Z. Naturforsch. 10a (1955) 177;
H.A. Bethe, Phys. Rev. 89 (1953) 1256.
[24] D.T. Cromer and J.T. Waber, Acta Crystallogr. 18 (1965) 104.